JACS
JOURNAL OF THE AMERICAN CHEMICAL SOCIETY
Article
pubs.acs.org/JACS

# Three-Bladed Rylene Propellers with Three-Dimensional Network Assembly for Organic Electronics

Dong Meng,[†,▽,#] Huiting Fu,[†,‡,▽,#] Chengyi Xiao,[†,▽] Xiangyi Meng,[∥] Thorsten Winands,[§] Wei Ma,[∥] Wei Wei,[⊥] Bingbing Fan,[‡] Lijun Huo,[‡] Nikos L. Doltsinis,[§] Yan Li,[*,†] Yanming Sun,[*,‡] and Zhaohui Wang[*,†]

[†]Beijing National Laboratory for Molecular Sciences, Key Laboratory of Organic Solids, Institute of Chemistry, Chinese Academy of Sciences, Beijing 100190, China

[‡]Heeger Beijing Research and Development Center, School of Chemistry and Environment, Beihang University, Beijing 100191, China

[§]Institute for Solid State Theory and Center for Multiscale Theory & Computation, University of Muenster, Wilhelm-Klemm-Strasse 10, 48149 Muenster, Germany

[∥]State Key Laboratory for Mechanical Behavior of Materials, Xi'an Jiaotong University, Xi'an 710049, China

[⊥]Department of Chemistry, Capital Normal University, Beijing 100048, China

[▽]University of Chinese Academy of Sciences, Beijing 100049, China

Supporting Information

**ABSTRACT:** Two kinds of conjugated $C_3$-symmetric perylene dyes, namely, triperylene hexaimides (TPH) and selenium-annulated triperylene hexaimides (TPH-Se), are efficiently synthesized. Both TPH and TPH-Se have broad and strong absorption in the region 300−600 nm together with suitable LUMO levels of about −3.8 eV. Single-crystal X-ray diffraction studies show that TPH displays an extremely twisted three-bladed propeller configuration and a unique 3D network assembly in which three PBI subunits in one TPH molecule have strong $\pi-\pi$ intermolecular interactions with PBI subunits in neighboring molecules. The integration of selenophene to TPH endows TPH-Se with a more distorted propeller configuration and a more compact 3D network assembly due to the Se···O interactions. A single-crystal transistor confirms that both TPH and TPH-Se possess good electron-transport ability. TPH and TPH-Se acceptor-based solar cells show high power conversion efficiency of 8.28% and 9.28%, respectively, which mainly results from the combined properties of broad and strong absorption ability, appropriate LUMO level, desirable aggregation, high electron mobility, and good film morphology with the polymer donor.

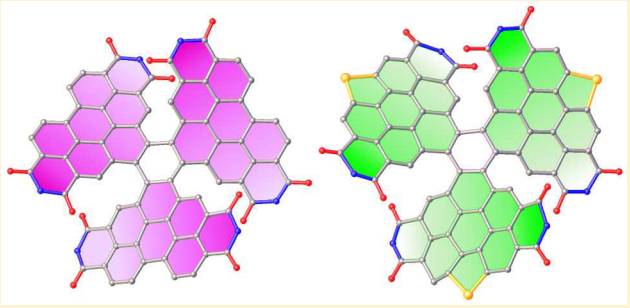

## INTRODUCTION

Over recent decades, rylene dyes containing extended conjugated skeletons have gained extensive attention due to their unique molecular structures, remarkable electro-optical properties, fascinating self-assembly behavior, and potential applications in various research fields as high-performance n-type organic semiconductors.[1] The elegant buildup of a homologous series of rylenes with the conjugated skeleton extension along the peri-positions has enabled a systematic variation of absorption and emission wavelengths reaching far into the near-infrared region.[2] Meanwhile, the lateral extension via both bay- and nonbay-functionalization to construct fully conjugated homologous and hybrid rylene arrays also induces tailored energy gaps and electron-accepting abilities.[3]

Recently, rylene dyes, especially perylene bisimides (PBIs), attracted much attention in bulk-heterojunction (BHJ) non-fullerene organic solar cells (OSCs).[4] In order to avoid large crystalline aggregate domains, various nonplanar perylene architectures were designed via functionalization in the bay or nonbay regions of PBIs and the imide groups.[5−8] Quite recently, we designed a series of bay-linked PBI dimers, and the power conversion efficiencies (PCEs) of BHJ organic solar cells based on them is up to 8.4% by incorporating heteroatoms into PBI bay regions.[9] Among PBI-based acceptors, most of them are linked via aromatic linkers, whereas PBI acceptors with large conjugated systems have a limited report and usually show relatively low performance.[10]

We are particularly interested in the design and synthesis of large conjugated systems based on rylene dyes. In our previous

**Received:** April 28, 2016
**Published:** July 21, 2016





DOI: 10.1021/jacs.6b04368
J. Am. Chem. Soc. 2016, 138, 10184−10190

works, various $\pi$-extended rylene dyes such as $\pi$-extended naphthalene diimides,[11] triply linked oligo-PBIs,[3a,b] hybrid rylene arrays,[3c] and thiophene annulated terrylene and quaterrylene diimides[12] were designed and synthesized via straightforward synthetic methodologies. Rylene dyes with large $\pi$-electron delocalization usually have broader and stronger absorption compared with unconjugated structures, whereas they usually display much lower LUMO levels. In order to obtain extended rylene dyes with suitable LUMO levels for OSC acceptors, rational molecular design strategies are very important.

In 2012, we first reported ethylene-annulated diPBIs, which displayed a much broader absorption spectrum compared with that of parent PBI.[13] We found that the introduction of an ethylene bridge could make the fused diPBIs with a suitable LUMO level close to that of $PC_{60}BM$ dominantly used as the acceptor in OSCs. Recently, Nuckolls and co-workers described a new synthetic procedure and obtained ethylene-annulated oligo-PBIs from dimer to tetramer, which proved to be a new class of highly efficient electron acceptors for OSCs.[14] Despite the great progress in one-dimensional conjugated PBIs, the development of high-performance OSC acceptors based on rylene dyes with rigid multidimensional architecture and a deep understanding of their optoelectronic properties and structure–assembly relationships are very important directions that the chemistry and material science communities work in.

Inspired by our previous works, herein, we present a new class of rigid three-dimensional (3D) rylene architectures that consist of three PBI subunits adjoining one single benzene ring. Two kinds of conjugated $C_3$-symmetric perylene dyes, namely, triperylene hexaimides (TPH) and selenium-annulated triperylene hexaimides (TPH-Se), are efficiently synthesized via Suzuki cross-coupling reaction and subsequent photocyclization. UV–vis absorption spectroscopy and cyclic voltammetry reveal that both TPH and TPH-Se have broad and strong absorption in the region 300–600 nm together with suitable LUMO levels of about −3.8 eV. Single-crystal X-ray diffraction studies show that TPH displays an extremely twisted three-bladed propeller configuration and a unique 3D network assembly in which three PBI subunits in one TPH molecule have strong $\pi$–$\pi$ intermolecular interactions with PBI subunits in neighboring molecules. The integration of selenophene to TPH endows TPH-Se with a more distorted propeller configuration and a more compact 3D network assembly due to the Se···O interactions. Single-crystal transistor characterization confirms that both TPH and TPH-Se possess good electron-transport ability. TPH and TPH-Se acceptor-based solar cells show high power conversion efficiency of 8.28% and 9.28%, respectively. The high photovoltaic performance mainly results from the combined properties of the acceptors, such as broad and strong light absorption ability, appropriate LUMO level, desirable aggregation, high electron mobility, and good film morphology with the polymer donor.

## RESULTS AND DISCUSSION

**Synthesis and Physical Properties.** The synthetic routes to $C_3$-symmetric TPH and TPH-Se are shown in Schemes 1 and 2. Monobromo-PBI **2** was obtained via bromination of PBI **1** according to known procedures developed by us.[9] Compound **3** was synthesized via a Suzuki coupling reaction between 1,3,5-benzenetriboronic acid tris(pinacol) ester and monobromo-PBI **2** using $Pd(PPh_3)_4$ as the catalyst. When compound **3** was dissolved in toluene containing a catalytic amount of $I_2$ and exposed to irradiation, TPH **4** was obtained in excellent yield. TPH-Se **6** was prepared in 87% yield via a one-pot procedure from the readily available precursor trinitro-triperylene hexaimides ($3NO_2$-TPH) **5**, synthesized by nitrification of TPH **4** at room temperature. The key step was carried out in *N*-methyl pyrrolidone (NMP) with Se powder at 190 °C for 12 h.

To investigate the structure–property relationships of the TPH skeleton, we selected two different substituents: a rigid side chain $CH_2C_3F_7$ and a flexible side chain $C_{11}H_{23}$. These compounds were fully characterized by high-resolution mass spectra and $^1H$ and $^{13}C$ NMR spectra. The target products **4**

**Scheme 1. Synthetic Route to Triperylene Hexaimides**[a]

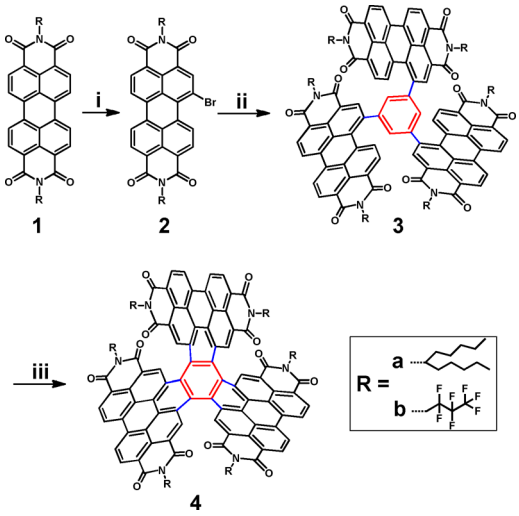


[a]Conditions: (i) For **2a**, $Br_2$, $CH_2Cl_2$, room temperature (rt); for **2b**, $Br_2$, conc $H_2SO_4$, 45 °C. Yields: 75% for **2a**; 71% for **2b**. (ii) 1,3,5-Benzenetriboronic acid tris(pinacol) ester, $Pd(PPh_3)_4$, $Na_2CO_3$ (2 M), THF, reflux. Yields: 91% for **3a**; 80% for **3b**. (iii) $h\nu$, $I_2$, toluene, rt. Yields: 93% for **4a**; 83% for **4b**.

**Scheme 2. Synthetic Route to Selenium-Annulated Triperylene Hexaimides**[b]

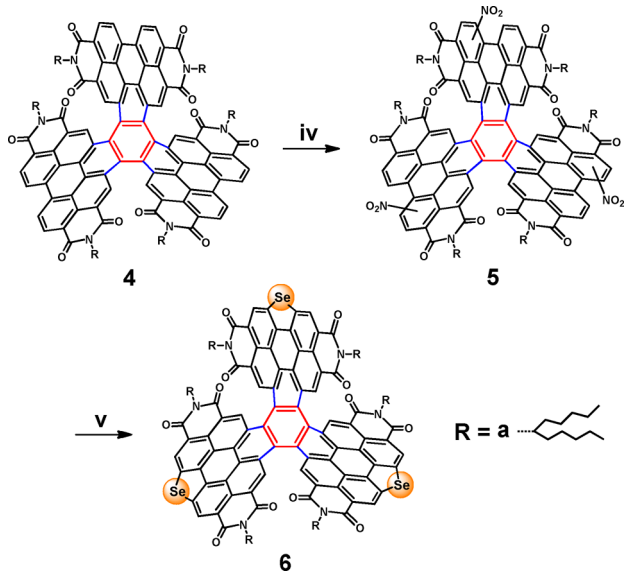


[b]Conditions: (iv) $CH_2Cl_2$, conc $HNO_3$, rt. Yield: 100%. (v) NMP, selenium powder, 190 °C. Yield: 87%.



DOI: 10.1021/jacs.6b04368
J. Am. Chem. Soc. 2016, 138, 10184–10190

and **6** are highly soluble in general organic solvents, such as dichloromethane, *ortho*-dichlorobenzene (*o*-DCB), and chloroform at room temperature. Such good solubility is mainly because of the nonplanar molecular scaffold. Considering that the TPH comprises three motifs of [5] helicene, we can depict four stereoisomers including two pairs of enantiomers (Figure S1b). However, it is very difficult to resolve racemates through the standard chiral HPLC (Figure S1c). The thermal properties were evaluated by thermal gravimetric analysis (TGA) performed under nitrogen. The target products **4a** and **6a** have the decomposition temperature of 5% weight loss above 380 °C (Figure S1a, SI).

The UV−vis absorption spectra of **1a**, **3a**, **4a**, **4b**, and **6a** in chloroform are shown in Figure 1a and Figure S3. Compound

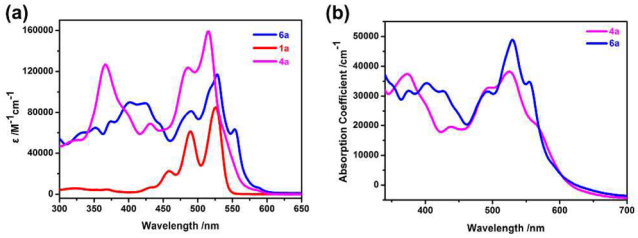


**Figure 1.** UV−vis absorption spectra of (a) **1a**, **4a**, and **6a** in $CHCl_3$ ($1 \times 10^{-5}$ M); (b) **4a** and **6a** films.

**3a** has a broad absorption in the range 400−600 nm with a maximum at 534 nm ($\varepsilon$ = 106 009 $M^{-1}$ $cm^{-1}$), similar to the absorption shape of parent **1a**. The spectrum of **4a** has a much higher absorptivity over the entire region 300−600 nm with two sharp maxima at 366 nm ($\varepsilon$ = 126 791 $M^{-1}$ $cm^{-1}$) and 516 nm ($\varepsilon$ = 159 007 $M^{-1}$ $cm^{-1}$), which is quite different from those of **1a** and **3a**. In comparison with **4a**, the maximum absorption of **6a** is red-shifted about 12 nm together with much broader and more complicated absorption waves. To determine how the PBI and the central benzene ring subunits interact to generate electronic behavior, quantum chemical calculations were performed using a time-dependent density functional theory (TDDFT) linear response method (see SI for computational details). Compared to **1a** and **3a**, the lowest energy peak of **4a** is blue-shifted by 10 and 18 nm, respectively. According to the TDDFT eigenvectors (Table S1), this peak predominantly arises from HOMO−LUMO transitions, where both the HOMO and the LUMO are 2-fold degenerate. The highest energy peak (around 360 nm), on the other hand, primarily involves transitions from the HOMO − 5, HOMO − 3, HOMO − 2, and HOMO to the LUMO, LUMO + 2, LUMO + 3, and LUMO + 4 (see Figure 2 and Figure S4), which are also quasidegenerate. Compared to **4a**, the lowest energy peak of **6a** is red-shifted by 12 nm and also arises from HOMO−LUMO transitions where HOMO and LUMO are 2-fold degenerate as well. One high-energy peak of **6a** is located at ∼360 nm, with another more distinct one at ∼400 nm. Relevant orbitals for those high-energy peaks are HOMO − 3, HOMO − 4, LUMO + 2, LUMO + 3, and LUMO + 4 (see Figure 2 and Table S1). While the frontier orbitals of **4a** and **6a** are strongly delocalized over the entire molecule, those of **3a** appear be localized on only one or two of the three PBI propellers. This explains why **4a** and **6a** absorb more strongly than **3a** in the high-energy region. For **3a**, according to the calculations, the dominant contribution in this region is at 381 nm due to transition from HOMO − 3 to LUMO (Table S1

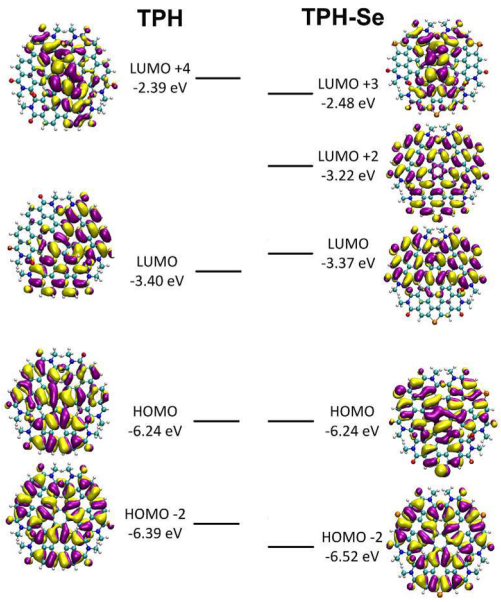


**Figure 2.** Energies and shapes of PBE0PBE/6-31G*/PCM frontier orbitals of model TPH and TPH-Se.

and Figure S5). Since these two orbitals are localized at opposite ends of the molecule, there is little overlap between them leading to a lower intensity. The absorption coefficients of **4a** and **6a** films were also measured (Figure 1b). Compound **6a** shows better light-absorbing capability than **4a** since its maximum absorption coefficient is 48 889 $cm^{-1}$ at 530 nm while the value of **4a** is 38 235 $cm^{-1}$ at 525 nm.

The electrochemical properties of **4** and **6** were studied by cyclic voltammetry in $CH_2Cl_2$, summarized in Table 1, and shown in Figure S2, together with the data of PBI **1a** for comparison. Compounds **4a** and **6a** both exhibit four reversible reduction waves with the first and second waves at −1.12, −1.15 V and −1.27, −1.31 V versus $Fc/Fc^+$, which are close to those of parent **1a** (−1.09 and −1.30 V) implying strong electron-accepting abilities. Compound **4b** exhibits three reversible reduction waves with the first and second waves at −0.96 and −1.13 V versus $Fc/Fc^+$ due to the introduction of fluorine alkyl chains to the imide groups. The LUMO values of **4a** and **6a** are estimated to be −3.83 and −3.80 eV from the onset reduction potential, which are a little higher than that of $PC_{60}BM$ (∼−3.90 eV).

**Single-Crystal Packing and Analysis.** To gain insight into molecular conformation of TPH and TPH-Se, we obtained the single crystals of **4b** and **6a** using the slow solvent vapor diffusion method.[15] As shown in Figure 3a, **4b** and **6a** present a "three-bladed propeller" conformation with the torsion angle $\alpha$ (25.10°, 26.96°, 32.97°) for **4b** and $\beta$ (25.47°, 28.67°, 41.55°) for **6a** due to the large steric encumbrance of the PBI subunits. Stunningly, the twisted propeller conformation warps the central benzene core with the torsion of about 22° for **4b** and 28° for **6a**. The torsion angle indicates that the molecular structure of TPH-Se **6a** is more twisted than **4b** probably owing to the selenium bridge which reduces the flexibility of configuration and thus increases the steric repulsion of PBI units. TPH **4b** and TPH-Se **6a** are both arranged in a slipped 3D stacking structure with similar $\pi-\pi$ intermolecular interactions of 3.31−3.45 Å for **4b** and 3.29−3.71 Å for **6a**. Meanwhile, obvious chalcogen bonding interactions of Se···O (ca. 3.0 Å) in TPH-Se **6a** between the adjacent molecules lead


DOI: 10.1021/jacs.6b04368
J. Am. Chem. Soc. 2016, 138, 10184−10190

**Table 1. Summary of Optical and Electronic Properties of 1a, 4a, 4b, and 6a in Solution**

| | $\lambda_{max}$ [a] [nm] | $\varepsilon$ [a] [$M^{-1}$ $cm^{-1}$] | $E_{1r}$ [b] [V] | $E_{2r}$ [b] [V] | $E_{LUMO}$ [c] [eV] | $E_{HOMO}$ [d] [eV] | $E_g$ [e] [eV] |
|---|---|---|---|---|---|---|---|
| **1a** | 526 | 85 136 | −1.09 | −1.30 | −3.88 | −6.17 | 2.29 |
| **4a** | 516 | 159 007 | −1.12 | −1.27 | −3.83 | −6.02 | 2.19 |
| **4b** | 514 | 127 993 | −0.96 | −1.13 | −4.04 | −6.22 | 2.18 |
| **6a** | 528 | 117 162 | −1.15 | −1.31 | −3.80 | −5.97 | 2.17 |

[a] $\lambda_{max}$ and $\varepsilon$ were measured in $CHCl_3$ ($1.0 \times 10^{-5}$ M). [b] Half-wave reductive potentials (in V vs $Fc/Fc^+$) measured in $CH_2Cl_2$ at a scan rate of 0.1 V/s using ferrocene as an internal potential mark. [c] Estimated from the onset potential of the first reduction wave and calculated according to $E_{LUMO} = -(4.8 + E_{onset}^{re})$ eV. [d] HOMO (eV) calculated according to $E_{HOMO} = (E_{LUMO} - E_g)$ eV. [e] Obtained from the edge of the absorption spectra in $CHCl_3$ solution according to $E_g = (1240/\lambda_{onset})$.

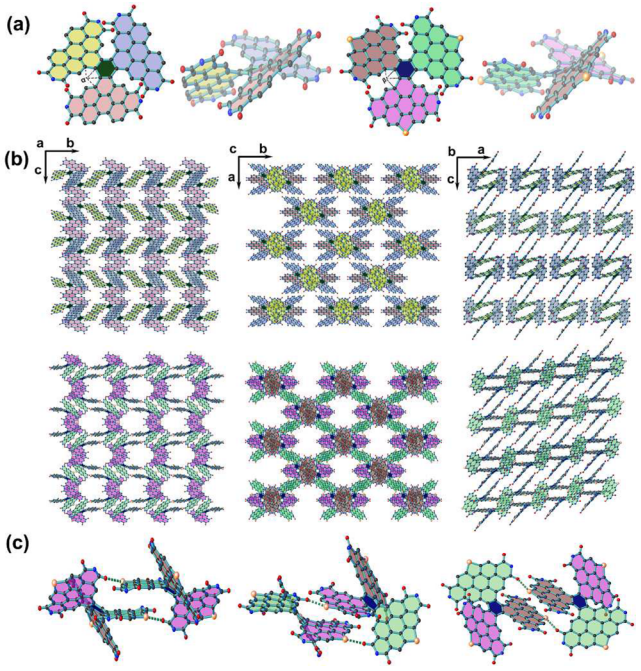


**Figure 3.** (a) X-ray molecular structures of TPH **4b** and TPH-Se **6a** (top view and side view). (The alkyl chains and hydrogen atoms are omitted for clarity.) (b) The slipped 3D stacking mode of TPH **4b** (top) and TPH-Se **6a** (down). (c) Se···O (3.0 Å) interactions between different PBI subunits of TPH-Se **6a**.

to the formation of closer packing (Figure 3b,c). Although there is a decrease in the intermolecular overlaps of each molecular skeleton in this slipped 3D stacking structure, the intermolecular interactions among the adjacent molecules are increased by the 3D interactions, which is beneficial for improving the carrier-transport properties. Due to their similarity to the fullerenes in terms of 3D transport properties, we speculate that target compounds **4** and **6** possess good carrier-transport and organic photovoltaic (OPV) properties. To this end, we fabricated the single-crystal transistor device and the photovoltaic device.

**Single-Crystal Transistor Characterization of TPH and TPH-Se.** Micro-/nanocrystals of TPH **4b** and TPH-Se **6a** were prepared by a facile in situ drop-coating method in which the semiconductor was dissolved in a chloroform solution. It is well-known that PBI derivatives with $CH_2C_3F_7$ substituents at the imide groups usually possess good charge-transport properties.[16] So, at the beginning, field-effect transistors (FETs) were constructed using **4b** micro-/nanocrystals as the semiconductor to probe its ability to transport electrons. FETs were fabricated on OTS modified $Si/SiO_2$ substrates using an "organic ribbon mask" technique.[17] The thickness of the micro-/nanocrystals of **4b** was 70−90 nm (Figure S6). Au was deposited on the micro-/nanocrystals as the source and drain electrodes as shown in Figure S6. Then, FETs using **6a** micro-/nanocrystals were also constructed using the same technique for comparison (Figure S7). The transfer and output characteristics of the FET devices based on **4b** and **6a** are shown in Figure 4. The FETs for **4b** exhibit the maximum

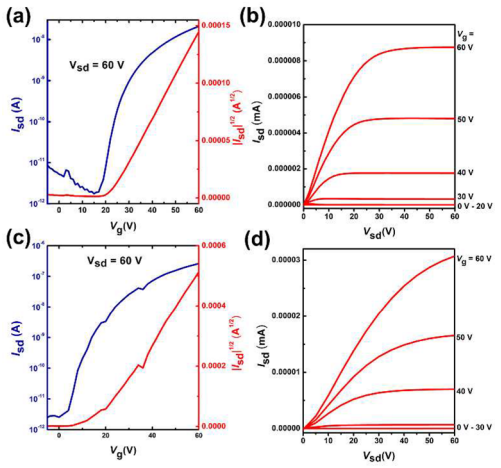


**Figure 4.** Typical transfer and output characteristics of micro-/nanocrystal OFETs based on (a, b) TPH **4b** and (c, d) TPH-Se **6a**.

electron mobility of 0.028 $cm^2$ $V^{-1}$ $s^{-1}$ whereas the FETs for **6a** also exhibit a high electron mobility of 0.032 $cm^2$ $V^{-1}$ $s^{-1}$. These results imply that, despite the substituents at the imide groups, both of these two propeller-shaped molecule skeletons could form compact 3D network channels facilitating electron transport.

**Photovoltaic Characterization of TPH and TPH-Se.** Solution-processed BHJ organic solar cells based on **4a** and **6a** were fabricated, where PDBT-T1 was used as the donor material (Figure S8a)[18] due to its complementary absorption (Figure S8b) and appropriately matched energy levels (Figure S8c) with **4a** and **6a**. The optimal D/A weight ratios were kept at 1:1 for all devices (Figure S9 and Table S2). The current density−voltage ($J$−$V$) characteristics of the optimal devices are shown in Figure 5a, and the device performance is shown in Table 2. For **4a**, a PCE of 7.34% was obtained, with an open-circuit voltage ($V_{OC}$) of 0.96 V, a short-circuit current ($J_{SC}$) of 11.75 mA/$cm^2$, and a fill factor (FF) of 65.3%. The devices based on **6a** showed an impressive PCE of 8.05%, with a $V_{OC}$ of 1.0 V, a $J_{SC}$ of 12.59 mA/$cm^2$, and an FF of 63.7%. One can find that both the $V_{OC}$ and the $J_{SC}$ values in solar cells based on **6a** are higher than those in the cells based on **4a**. The higher $V_{OC}$ is because of the higher-lying LUMO level of **6a**. In order to further optimize the cell performance, 1,8-diiodooctane (DIO)


DOI: 10.1021/jacs.6b04368
J. Am. Chem. Soc. 2016, 138, 10184−10190

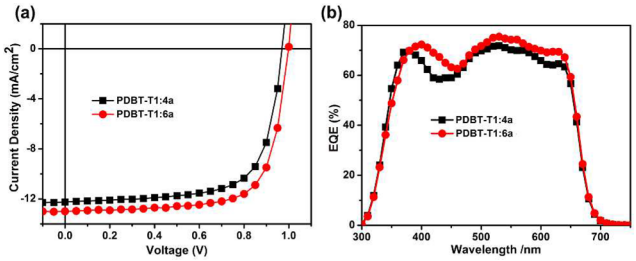


**Figure 5.** (a) $J-V$ curves of solar cells based on PDBT-T1:**4a** with 0.25% DIO and PDBT-T1:**6a** with 0.75% DIO and (b) the corresponding EQE spectra.

was employed as the solvent additive (as shown in Figure S10 and Table S3 and S4). When 0.25% DIO was used, the $J_{SC}$ and FF of devices based on **4a** are simultaneously increased, resulting in an enhanced PCE of 8.28%. Likewise, the DIO has a positive influence on the device performance of **6a**. With the addition of 0.75% DIO, the devices yield the best PCE of 9.28%, with a $V_{OC}$ of 1.0 V, a $J_{SC}$ of 12.99 mA/cm$^2$, and a high FF of 71.5%. To the best of our knowledge, this efficiency is the highest value reported so far for organic solar cells fabricated with PBI-based acceptor material. The results demonstrate that **4a** and **6a** are promising nonfullerene acceptors for application in highly efficient OSCs.

The external quantum efficiency (EQE) plots of solar cells based on **4a** and **6a** are shown in Figure 5b. The EQE curves of **4a**- and **6a**-based devices cover a broad spectral response from 300 to 700 nm. The EQE values of PDBT-T1:**6a** solar cell are higher than those of the device with **4a** in the wavelength range 380−650 nm, indicating that the PDBT-T1:**6a** system exhibits more efficient incident photon-to-current conversion efficiency compared with the PDBT-T1:**4a** system. The calculated $J_{SC}$ integrated from the EQE spectra for devices based on **4a** and **6a** are 11.78 and 12.41 mA/cm$^2$, respectively, agreeing well with those measured from $J-V$ curves. The space-charge-limited-current (SCLC) method was performed to investigate the bulk charge-transport properties of the optimal blend films (see Figure S11).[19] For the PDBT-T1:**4a** blend film, the electron and hole mobilities are $1.5 \times 10^{-3}$ and $1.0 \times 10^{-3}$ cm$^2$ V$^{-1}$ s$^{-1}$, respectively ($\mu_e/\mu_h$ = 1.5). For a PDBT-T1:**6a** blend film, the electron mobily is $2.2 \times 10^{-3}$ cm$^2$ V$^{-1}$ s$^{-1}$, and the hole mobility is $1.7 \times 10^{-3}$ cm$^2$ V$^{-1}$ s$^{-1}$ ($\mu_e/\mu_h$ = 1.3). The electron mobilities in neat **4a** and **6a** films were also measured (see Figure S12). Both **4a** and **6a** possess good electron-transport properties, whereas the electron mobility of **4a** ($2.4 \times 10^{-3}$ cm$^2$ V$^{-1}$ s$^{-1}$) is slightly lower than that of **6a** ($3.2 \times 10^{-3}$ cm$^2$ V$^{-1}$ s$^{-1}$). The higher carrier mobilities and more balanced carrier transport may partially explain the better solar cell performance observed in the **6a**-based solar cells than that of **4a**-based solar cells.

To gain insight into the morphology of **4a** and **6a** films, atomic force microscopy (AFM) was carried out. As shown in Figure S13, neat **4a** has a relatively coarse surface with a root-mean-square (RMS) of 4.78 nm, while quite smooth and uniform surfaces were observed for neat **6a** with an RMS of 0.60 nm. Without using DIO, PDBT-T1:**4a** and PDBT-T1:**6a** films show uniform surfaces with an RMS of 1.11 and 0.86 nm, respectively, and the fibrous features were clearly seen in such films. With incorporating a small amount of DIO, the blend films still showed the fibrous feature, but with a rougher surface with an RMS value of 1.48 and 0.89 nm for PDBT-T1:**4a** and PDBT-T1:**6a**, respectively. The results indicated that DIO induced the aggregation of PDBT-T1 donor and resulted in higher device performance.

To further understand the different photovoltaic performance of the blend films and the role of the DIO, grazing-incidence wide-angle X-ray scattering (GIWAXS) and resonate soft X-ray scattering (R-SoXS) measurements were carried out to reveal the molecular packing and the phase separation of the active layers. The 2D GIWAXS patterns and the corresponding out-of-plane and in-plane line cuts are presented in Figure 6.

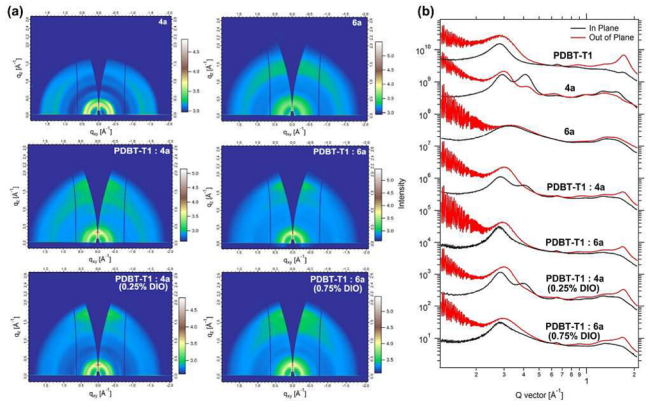


**Figure 6.** (a) Two-dimensional GIWAXS patterns and (b) scattering profiles out-of-plane and in-plane for neat **4a**, **6a** films and PDBT-T1:**4a** without and with 0.25% DIO and PDBT-T1:**6a** without and with 0.75% DIO.

The neat PDBT-T1 film shows an obvious (100) lamellar diffraction peak at $q_{xy} \approx 0.28$ Å$^{-1}$ ($d \approx 22.4$ Å). A strong (010) $\pi-\pi$ stacking peak is observed in the out-of-plane direction at $q \approx 1.72$ Å$^{-1}$ ($d \approx 3.65$ Å), suggesting that a face-on molecular orientation on the substrate of the PDBT-T1 dominated. Both of the two pure acceptors show (100) reflection peaks at about 0.29 and 0.32 Å$^{-1}$ for **4a** and **6a**, respectively, implying that the selenium-annulated units makes the tighter of lamellar packing. In the in-plane direction, a diffraction peak at 0.42 Å$^{-1}$ was the (001) peak, corresponding to the distance (14.95 Å) of two PBI subunits in neighboring **4a** molecules. However, the crystallinity of **6a** was found to be much weaker than **4a**, since no $\pi-\pi$ stacking peak was observed both in the in-plane and out-of-plane directions; meanwhile, the intensity of the lamellar

**Table 2. Device Performance of BHJ Organic Solar Cells Fabricated with 4a and 6a.**

| | DIO [%] | $V_{oc}$ [V] | $J_{sc}$ [mA/cm$^2$] | FF [%] | PCE[a] [%] | PCE$_{max}$ [%] |
|---|---|---|---|---|---|---|
| **4a** | 0 | 0.961 ± 0.003 | 11.71 ± 0.05 | 64.8 ± 0.6 | 7.28 ± 0.07 | 7.34 |
| | 0.25 | 0.968 ± 0.002 | 12.01 ± 0.19 | 70.1 ± 0.3 | 8.15 ± 0.14 | 8.28 |
| **6a** | 0 | 1.007 ± 0.003 | 12.32 ± 0.17 | 63.9 ± 0.8 | 7.93 ± 0.09 | 8.05 |
| | 0.75 | 1.001 ± 0.004 | 12.53 ± 0.19 | 71.7 ± 0.4 | 8.98 ± 0.12 | 9.28 |

[a]The efficiency value was calculated from six devices.



DOI: 10.1021/jacs.6b04368
J. Am. Chem. Soc. 2016, 138, 10184−10190

packing was relatively low. The results agree well with the data of single crystals, where **6a** shows a more twisted structure than **4a**. When blended with **4a** or **6a**, the $\pi-\pi$ stacking peak of PDBT-T1 out-of-plane is quite weak, and the two blends processed without DIO exhibit the (010) peak at a same location of $q \approx 1.71$ Å$^{-1}$. The coherence length of the (010) $\pi-\pi$ stacking can be calculated by the Scherrer equation. The coherence length for the **4a** and **6a** blend films processed with DIO is 28.5 and 30 Å, and 26.8 Å for the neat PDBT-T1, respectively. This suggests that, by incorporating a small amount of DIO, the crystallinity of PDBT-T1 becomes stronger, which reveals that the DIO facilitates the face-on orientation of PDBT-T1 in blend films, giving rise to improved vertical charge transport and thus increased $J_{sc}$ and FF. R-SoXS data were acquired at 285.2 eV, at which point the contrast between the PDBT-T1 and the acceptor is enhanced. R-SoXS results confirm that the domain spacing formed in the optimal PDBT-T1:**6a** film (14.20 nm) is slightly smaller than that in the optimal PDBT-T1:**4a** film (14.70 nm) (Figure S14). The small domain size is beneficial to exciton separation. This may partially account for the reason that both **4a** and **6a** exhibit excellent photovoltaic performance.

## CONCLUSION

In summary, we have designed and efficiently synthesized novel n-type organic semiconductors based on rylene dyes with rigid and conjugated architecture. These two kinds of rylene semiconductors, TPH and TPH-Se, display extremely twisted three-bladed propeller configuration and form compact 3D network assembly in which the three PBI subunits have strong $\pi-\pi$ intermolecular interactions with other PBI subunits in neighboring molecules. Single-crystal transistor characterizations confirm that these compact 3D networks could provide an effective electron-transport channel. TPH and TPH-Se acceptor-based solar cells show high power conversion efficiency of 8.28% and 9.28%, respectively, which are the highest values that have been reported for PBI acceptors. The high photovoltaic performance mainly results from the combined properties of the acceptors, such as broad and strong light absorption ability, appropriate LUMO level, desirable aggregation, high electron mobility, and good film morphology with the polymer donor. The deep understanding of their optoelectronic properties and structure–property relationships will provide guidance for the design of high-performance n-type semiconductors for organic electronics.

## ASSOCIATED CONTENT

### Supporting Information

The Supporting Information is available free of charge on the ACS Publications website at DOI: 10.1021/jacs.6b04368.

Experimental details, synthesis and characterizations, TGA curves, X-ray data, theoretical calculations, UV absorption, device fabrication and characterizations, cyclic voltammogram measurement, SCLC measurements, AFM images and R-SoXS profiles (PDF)
Crystal information for TPH **4b** (CIF)
Crystal information for TPH-Se **6a** (CIF)

## AUTHOR INFORMATION


### Corresponding Authors

*yanli@iccas.ac.cn
*sunym@buaa.edu.cn
*wangzhaohui@iccas.ac.cn

### Author Contributions

#D.M. and H.F. contributed equally.


### Notes

The authors declare no competing financial interest.

## ACKNOWLEDGMENTS

This work was financially supported by the National Natural Science Foundation of China (NSFC) (nos. 21225209, 91427303, 21190032, 51473009), the 973 Program (2012CB932903), NSFC-DFG joint project TRR61 (21261130581), the Chinese Academy of Sciences (XDB12010100), and the International Science & Technology Cooperation Program of China (no. 2014DFA52820). The authors gratefully acknowledge the following people: Prof. W. Hu of Tianjin University for the single-crystal transistor characterization, Prof. X. Deng of Beijing Normal University for their assistance with single-crystal measurements and refinement, and Prof. Y. Fan of Beihang University for the assistance with AFM measurements. X-ray data was acquired at beamlines 7.3.3 at the Advanced Light Source, which is supported by the Director, Office of Science, Office of Basic Energy Sciences, of the U.S. Department of Energy under Contract No. DE-AC02-05CH11231.

## REFERENCES


(1) (a) Jiang, W.; Li, Y.; Wang, Z. *Acc. Chem. Res.* **2014**, *47*, 3135–3147. (b) Ball, M.; Zhong, Y.; Wu, Y.; Schenck, C.; Ng, F.; Steigerwald, M.; Xiao, S.; Nuckolls, C. *Acc. Chem. Res.* **2015**, *48*, 267–276.

(2) (a) Pschirer, N. G.; Kohl, C.; Nolde, F.; Qu, J.; Müllen, K. *Angew. Chem., Int. Ed.* **2006**, *45*, 1401–1404. (b) Yuan, Z.; Lee, S.-L.; Chen, L.; Li, C.; Mali, K. S.; De Feyter, S.; Müllen, K. *Chem. - Eur. J.* **2013**, *19*, 11842–11846. (c) Weil, T.; Vosch, T.; Hofkens, J.; Peneva, K.; Müllen, K. *Angew. Chem., Int. Ed.* **2010**, *49*, 9068–9093. (d) Langhals, H.; Schönmann, G.; Feiler, L. *Tetrahedron Lett.* **1995**, *36*, 6423–6424. (e) Langhals, H.; Zgela, D.; Lüling, R. *J. Org. Chem.* **2015**, *80*, 12146–12150.

(3) (a) Qian, H.; Wang, Z.; Yue, W.; Zhu, D. *J. Am. Chem. Soc.* **2007**, *129*, 10664–10665. (b) Qian, H.; Negri, F.; Wang, C.; Wang, Z. *J. Am. Chem. Soc.* **2008**, *130*, 17970–17976. (c) Yue, W.; Lv, A.; Gao, J.; Jiang, W.; Hao, L.; Li, C.; Li, Y.; Polander, L. E.; Barlow, S.; Hu, W.; Di Motta, S.; Negri, F.; Marder, S. R.; Wang, Z. *J. Am. Chem. Soc.* **2012**, *134*, 5770–5773.

(4) (a) Li, C.; Wonneberger, H. *Adv. Mater.* **2012**, *24*, 613–636. (b) Nielsen, C. B.; Holliday, S.; Chen, H.-Y.; Cryer, S. J.; McCulloch, I. *Acc. Chem. Res.* **2015**, *48*, 2803–2812.

(5) (a) Hartnett, P. E.; Timalsina, A.; Ramakrishna Matte, H. S. S.; Zhou, N.; Guo, X.; Zhao, W.; Facchetti, A.; Chang, R. P. H.; Hersam, M. C.; Wasielewski, M. R.; Marks, T. J. *J. Am. Chem. Soc.* **2014**, *136*, 16345–16356. (b) Cai, Y.; Huo, L.; Sun, X.; Wei, D.; Tang, M.; Sun, Y. *Adv. Energy Mater.* **2015**, *5*, 1500032.

(6) (a) Rajaram, S.; Shivanna, R.; Kandappa, S. K.; Narayan, K. S. *J. Phys. Chem. Lett.* **2012**, *3*, 2405–2408. (b) Wu, C.-H.; Chueh, C.-C.; Xi, Y.-Y.; Zhong, H.-L.; Gao, G.-P.; Wang, Z.-H.; Pozzo, L. D.; Wen, T.-C.; Jen, A. K. Y. *Adv. Funct. Mater.* **2015**, *25*, 5326–5332. (c) Ye, L.; Sun, K.; Jiang, W.; Zhang, S.; Zhao, W.; Yao, H.; Wang, Z.; Hou, J. *ACS Appl. Mater. Interfaces* **2015**, *7*, 9274–9280.

(7) (a) Yan, Q.; Zhou, Y.; Zheng, Y.-Q.; Pei, J.; Zhao, D. *Chem. Sci.* **2013**, *4*, 4389–4394. (b) Zhang, X.; Lu, Z.; Ye, L.; Zhan, C.; Hou, J.; Zhang, S.; Jiang, B.; Zhao, Y.; Huang, J.; Zhang, S.; Liu, Y.; Shi, Q.; Liu, Y.; Yao, J. *Adv. Mater.* **2013**, *25*, 5791–5797.

(8) Liu, Y.; Mu, C.; Jiang, K.; Zhao, J.; Li, Y.; Zhang, L.; Li, Z.; Lai, J. Y. L.; Hu, H.; Ma, T.; Hu, R.; Yu, D.; Huang, X.; Tang, B. Z.; Yan, H. *Adv. Mater.* **2015**, *27*, 1015–1020.




DOI: 10.1021/jacs.6b04368
J. Am. Chem. Soc. 2016, 138, 10184–10190

(9) (a) Meng, D.; Sun, D.; Zhong, C.; Liu, T.; Fan, B.; Huo, L.; Li, Y.; Jiang, W.; Choi, H.; Kim, T.; Kim, J. Y.; Sun, Y.; Wang, Z.; Heeger, A. J. *J. Am. Chem. Soc.* **2016**, *138*, 375−380. (b) Sun, D.; Meng, D.; Cai, Y.; Fan, B.; Li, Y.; Jiang, W.; Huo, L.; Sun, Y.; Wang, Z. *J. Am. Chem. Soc.* **2015**, *137*, 11156−11162.
(10) (a) Zhong, H.; Wu, C.-H.; Li, C.-Z.; Carpenter, J.; Chueh, C.-C.; Chen, J.-Y.; Ade, H.; Jen, A. K.-Y. *Adv. Mater.* **2016**, *28*, 951−958. (b) Hartnett, P. E.; Ramakrishna Matte, H. S. S.; Eastham, N. D.; Jackson, N. E.; Wu, Y.; Chen, L. X.; Ratner, M. A.; Chang, R. P. H.; Hersam, M. C.; Wasielewski, M. R.; Marks, T. J. *Chem. Sci.* **2016**, *7*, 3543−3555.
(11) (a) Yue, W.; Gao, J.; Li, Y.; Jiang, W.; Di Motta, S.; Negri, F.; Wang, Z. *J. Am. Chem. Soc.* **2011**, *133*, 18054−18057. (b) Gao, J.; Li, Y.; Wang, Z. *Org. Lett.* **2013**, *15*, 1366−1369. (c) Li, C.; Xiao, C.; Li, Y.; Wang, Z. *Org. Lett.* **2013**, *15*, 682−685. (d) Li, C.; Lin, Z.; Li, Y.; Wang, Z. *Chem. Rec.* **2016**, *16*, 873−885.
(12) Li, Y.; Xu, W.; Di Motta, S.; Negri, F.; Zhu, D.; Wang, Z. *Chem. Commun.* **2012**, *48*, 8204−8206.
(13) Li, Y.; Wang, C.; Li, C.; Di Motta, S.; Negri, F.; Wang, Z. *Org. Lett.* **2012**, *14*, 5278−5281.
(14) (a) Zhong, Y.; Trinh, M. T.; Chen, R.; Purdum, G. E.; Khlyabich, P. P.; Sezen, M.; Oh, S.; Zhu, H.; Fowler, B.; Zhang, B.; Wang, W.; Nam, C.-Y.; Sfeir, M. Y.; Black, C. T.; Steigerwald, M. L.; Loo, Y.-L.; Ng, F.; Zhu, X.-Y.; Nuckolls, C. *Nat. Commun.* **2015**, *6*, 8242. (b) Zhong, Y.; Kumar, B.; Oh, S.; Trinh, M. T.; Wu, Y.; Elbert, K.; Li, P.; Zhu, X.; Xiao, S.; Ng, F.; Steigerwald, M. L.; Nuckolls, C. *J. Am. Chem. Soc.* **2014**, *136*, 8122−8130.
(15) Although the single crystals of **4b** and **6a** were measured at low temperature, 100 and 170 K, to prevent unfavorable effect from the molecular vibration, the disorder remains in the side chain attached to each nitrogen atom. To solve this problem, we used the squeeze method to dissolve the disorder in the side chains, which resulted in a relatively large *R* value (0.19 and 0.17). Fortunately, the diffraction from the conjugated backbone could be easily confirmed, and we did not find any errors from the conjugated backbone. Meanwhile, because **4b** and **6a** both crystallize in the centrosymmetric space group *C*2/*c*, they form racemic crystals that contain equal amounts of (*P*, *P*, *P*) and (*M*, *M*, *M*) forms (Figure S1b).
(16) (a) Li, Y.; Tan, L.; Wang, Z.; Qian, H.; Shi, Y.; Hu, W. *Org. Lett.* **2008**, *10*, 529−532. (b) Li, Y.; Li, C.; Yue, W.; Jiang, W.; Kopecek, R.; Qu, J.; Wang, Z. *Org. Lett.* **2010**, *12*, 2374−2377. (c) Liu, C.; Xiao, C.; Li, Y.; Hu, W.; Li, Z.; Wang, Z. *Chem. Commun.* **2014**, *50*, 12462−12464.
(17) Jiang, L.; Gao, J.; Wang, E.; Li, H.; Wang, Z.; Hu, W.; Jiang, L. *Adv. Mater.* **2008**, *20*, 2735−2740.
(18) Huo, L.; Liu, T.; Sun, X.; Cai, Y.; Heeger, A. J.; Sun, Y. *Adv. Mater.* **2015**, *27*, 2938−2944.
(19) Malliaras, G. G.; Salem, J. R.; Brock, P. J.; Scott, C. *Phys. Rev. B: Condens. Matter Mater. Phys.* **1998**, *58*, R13411.


DOI: 10.1021/jacs.6b04368
*J. Am. Chem. Soc.* 2016, 138, 10184−10190